

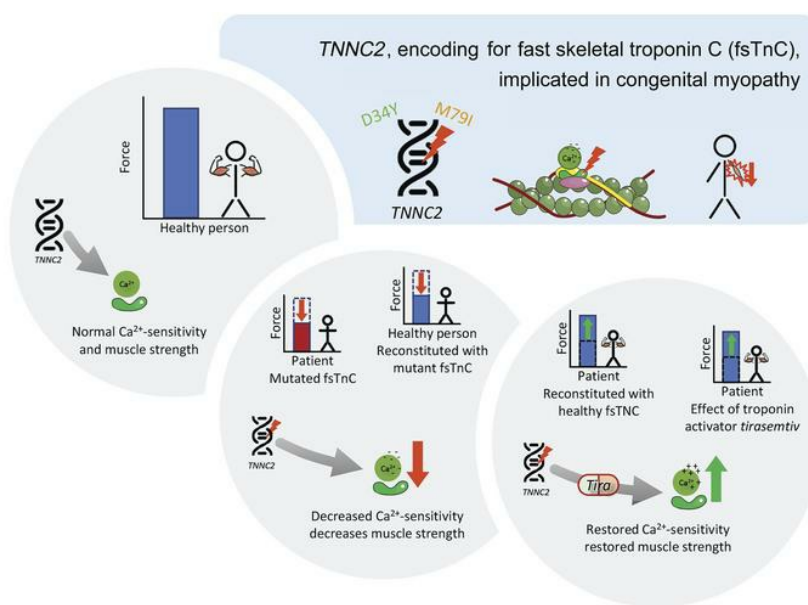
Pathogenic variants in *TNNC2* cause congenital myopathy due to an impaired force response to calcium

Martijn van de Locht, ... , Carsten G. Bönnemann, Coen A.C. Ottenheijm

J Clin Invest. 2021;131(9):e145700. <https://doi.org/10.1172/JCI145700>.

Research Article Genetics Muscle biology

Graphical abstract



Find the latest version:

<https://jci.me/145700/pdf>



Pathogenic variants in *TNNC2* cause congenital myopathy due to an impaired force response to calcium

Martijn van de Locht,¹ Sandra Donkervoort,² Josine M. de Winter,¹ Stefan Conijn,¹ Leon Begthel,¹ Benno Kusters,³

Payam Mohassel,² Ying Hu,² Livija Medne,⁴ Colin Quinn,⁵ Steven A. Moore,⁶ A. Reghan Foley,² Gwimoon Seo,⁷ Darren T. Hwee,⁸

Fady I. Malik,⁸ Thomas Irving,⁹ Weikang Ma,⁹ Henk L. Granzier,¹⁰ Erik-Jan Kamsteeg,³ Kalyan Immadisetty,¹¹

Peter Kekenes-Huskey,¹¹ José R. Pinto,¹² Nicol Voermans,³ Carsten G. Bönnemann,² and Coen A.C. Ottenheijm^{1,10}

¹Department of Physiology, Amsterdam UMC (location VUmc), Amsterdam, Netherlands. ²Neuromuscular and Neurogenetic Disorders of Childhood Section, National Institute of Neurological Disorders and Stroke, NIH, Bethesda, Maryland, USA. ³Department of Neurology and Human Genetics, Radboud University Medical Center, Nijmegen, Netherlands. ⁴Division of Human Genetics, Department of Pediatrics, Individualized Medical Genetics Center, Children's Hospital of Philadelphia, Philadelphia, Pennsylvania, USA. ⁵Department of Neurology, University of Pennsylvania, Philadelphia, Pennsylvania, USA. ⁶Department of Pathology, University of Iowa Carver College of Medicine, Iowa City, Iowa, USA. ⁷Protein Expression Facility, Institute of Molecular Biophysics, The Florida State University, Tallahassee, Florida, USA. ⁸Research and Early Development, Cytokinetics Inc., South San Francisco, California, USA. ⁹BioCAT, Illinois Institute of Technology, Chicago, Illinois, USA. ¹⁰Department of Cellular and Molecular Medicine, University of Arizona, Tucson, Arizona, USA. ¹¹Department of Cell and Molecular Physiology, Loyola University, Chicago, Illinois, USA. ¹²Department of Biomedical Sciences, The Florida State University College of Medicine, Tallahassee, Florida, USA.

Troponin C (TnC) is a critical regulator of skeletal muscle contraction; it binds Ca^{2+} to activate muscle contraction.

Surprisingly, the gene encoding fast skeletal TnC (*TNNC2*) has not yet been implicated in muscle disease. Here, we report 2 families with pathogenic variants in *TNNC2*. Patients present with a distinct, dominantly inherited congenital muscle disease. Molecular dynamics simulations suggested that the pathomechanisms by which the variants cause muscle disease include disruption of the binding sites for Ca^{2+} and for troponin I. In line with these findings, physiological studies in myofibers isolated from patients' biopsies revealed a markedly reduced force response of the sarcomeres to $[\text{Ca}^{2+}]$. This pathomechanism was further confirmed in experiments in which contractile dysfunction was evoked by replacing TnC in myofibers from healthy control subjects with recombinant, mutant TnC. Conversely, the contractile dysfunction of myofibers from patients was repaired by replacing endogenous, mutant TnC with recombinant, wild-type TnC. Finally, we tested the therapeutic potential of the fast skeletal muscle troponin activator tirasemtiv in patients' myofibers and showed that the contractile dysfunction was repaired. Thus, our data reveal that pathogenic variants in *TNNC2* cause congenital muscle disease, and they provide therapeutic angles to repair muscle contractility.

Introduction

Skeletal muscle cells (myofibers) are densely packed with myofibrils, which consist of repeating structural units named sarcomeres (Figure 1A). Sarcomeres, the contractile units of muscle, are composed of thick filaments that contain the motor protein myosin and thin filaments composed of double helical strands of actin monomers, a coiled-coil dimer strand of tropomyosin, and the troponin (Tn) complex (Figure 1B).

The Tn complex is a critical regulator of contraction. It is composed of 3 distinct subunits named according to their functions: a highly conserved Ca^{2+} -binding subunit (TnC); an actomyosin ATPase inhibitory subunit (TnI), and a tropomyosin-binding subunit (TnT). When muscle is activated, Ca^{2+} enters the cytosol, starting a molecular dance between the thick and thin filaments (1). First, Ca^{2+} binds to TnC, which initiates a chain of events in

the other Tn subunits and leads to movement of the tropomyosin molecule, a process also modulated by myosin-binding protein C (2). This movement exposes myosin-binding sites on actin and allows the myosin heads on the thick filament to grab and pull on the actin molecules, thereby generating force. This ceaseless cycle is the mechanical basis for muscle contraction. Thus, TnC plays a gatekeeper role in transmitting the Ca^{2+} signal to other sarcomere proteins to activate muscle contraction.

To date, the gene encoding fast skeletal TnC (fsTnC) (*TNNC2*; the skeletal muscle-specific TnC isoform) has not been implicated in any muscle disease (myopathy). This is surprising, considering that TnC plays a key role in muscle contraction, and that nearly all other genes encoding key proteins in the sarcomere have been linked to disease, some already decades ago (3). Here, we resolve this enigma and report 2 unrelated families with pathogenic variants in *TNNC2*. Patients present with a distinct, dominantly inherited congenital myopathy, notable for polyhydramnios during gestational development, and congenital weakness and severe respiratory muscle involvement with clinical improvement over time. The latter is atypical for congenital myopathy, which often has a static or progressive nature. Molecular dynamics (MD) simulations indicated that the *TNNC2* variants perturb the dynamics of the TnC regions responsible for Ca^{2+} binding and

Authorship note: CGB and CACO contributed equally to this work.

Conflict of interest: The authors have declared that no conflict of interest exists.

Copyright: © 2021, American Society for Clinical Investigation.

Submitted: November 10, 2020; **Accepted:** March 18, 2021; **Published:** May 3, 2021.

Reference information: *J Clin Invest.* 2021;131(9):e145700.

<https://doi.org/10.1172/JCI145700>.

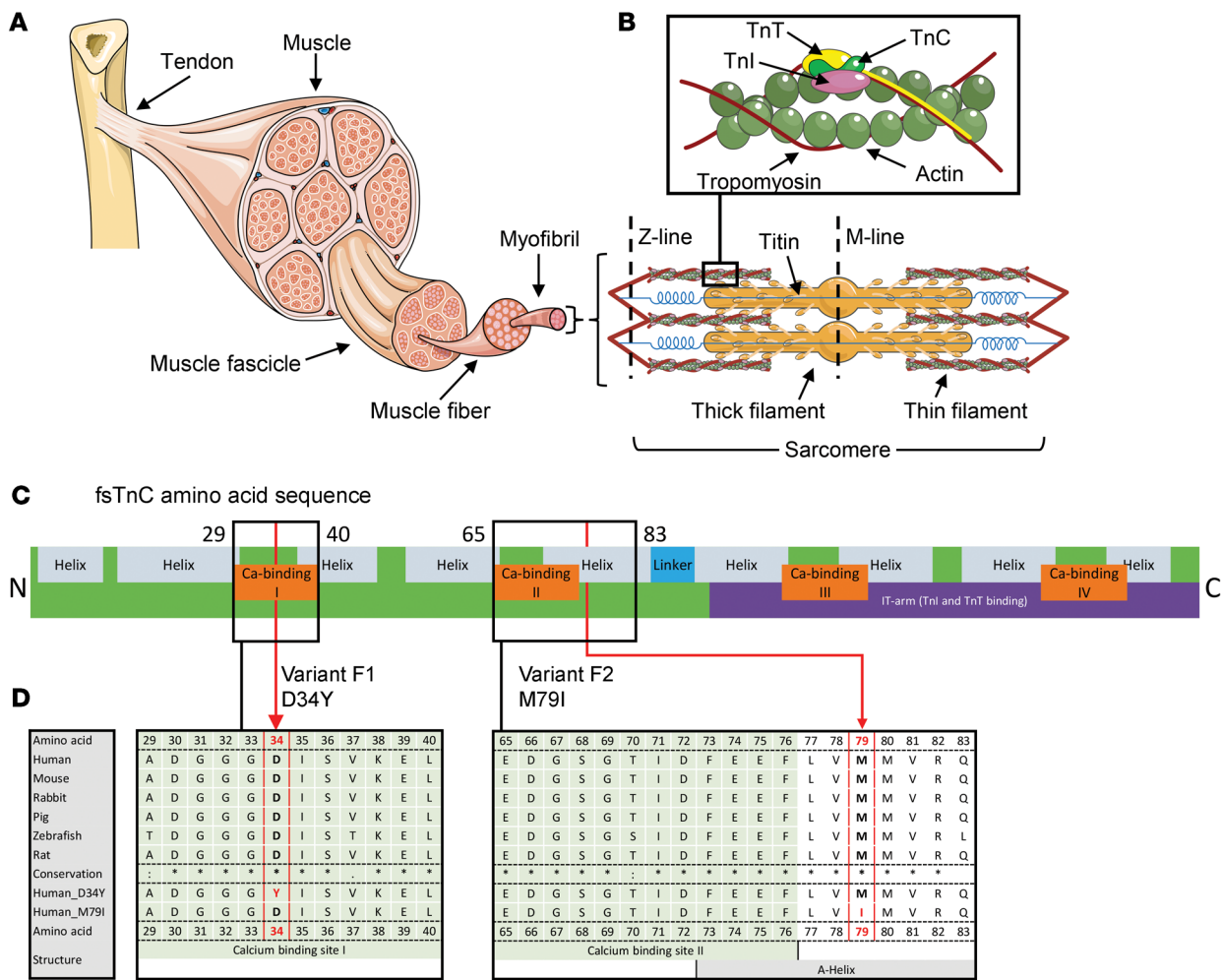


Figure 1. Muscle structure. (A) Sarcomeres are the smallest contractile units in muscle, consisting of myosin-based thick filaments and actin-based thin filaments decorated with the regulatory proteins troponin (Tn) and tropomyosin. (B) Magnification of the Tn complex, consisting of TnC, TnT, and TnI, and tropomyosin on the actin-based thin filament. The images are modified from Servier Medical ART, licensed under a Creative Commons Attribution 3.0 generic license (58). (C) Schematic representation of the amino acid sequence of fsTnC; N = N-terminus; C = C-terminus. Both patient variants are indicated [F1:P1, c.100G>T, p.(Asp34Tyr), D34Y; F2:P1, c.237G>C, p.(Met79Ile), M79I]. (D) Alignment of the fsTnC amino acid sequence in various species. The mutated residues are outlined in red.

for binding of the TnI switch peptide. In line with the findings from the MD simulations, studies in myofibers isolated from patients' biopsies revealed that the muscle weakness is caused by a reduced force response of the sarcomeres to submaximal $[Ca^{2+}]$. The pathogenicity of the variants was established in experiments, in which this contractile dysfunction was evoked by replacing endogenous TnC in myofibers from healthy control subjects with recombinant, mutant TnC. Conversely, we could repair the contractile dysfunction of myofibers from patients by replacing endogenous, mutant TnC with recombinant, wild-type (WT) TnC. Finally, we tested the therapeutic potential of the fast skeletal muscle Tn activator tirasemtiv in patients' myofibers and showed that the contractile dysfunction was repaired.

Results

Clinical presentation

Detailed clinical information for all patients is described in Table 1 and a full description of the patients is provided in the Supplemental Results (supplemental material available online with this article;

<https://doi.org/10.1172/JCI145700DS1>). Figure 2 shows family pedigrees, clinical and MRI images, and the visualization of muscle weakness (MuscleViz; based on the Medical Research Council grading). In brief, this disorder presents as a dominantly inherited myopathy with a characteristic clinical phenotype defining it as congenital in presentation. Distinct phenotypic characteristics include polyhydramnios during gestation, weakness, and severe respiratory muscle involvement in the immediate postnatal period followed by clinical improvement over time with nonobligatory external ophthalmoparesis.

Identification of *TNNC2* variants

In both families, whole-exome sequencing (WES) did not identify pathogenic variants in any of the known neuromuscular disease genes (details in Methods section). Subsequent analysis identified in family 1 (patient 1 [P1], P2, and P3) a heterozygous variant in *TNNC2*, encoding fsTnC: c.100G>T; p.(Asp34Tyr); hereafter referred to as D34Y. The variant was predicted to be damaging and was not present in dbSNP, NHLBI EVS, or gnomAD (covering >125,000 individuals). The variant was confirmed through Sanger

Table 1. Detailed clinical description of family 1 (F1) and family 2 (F2)

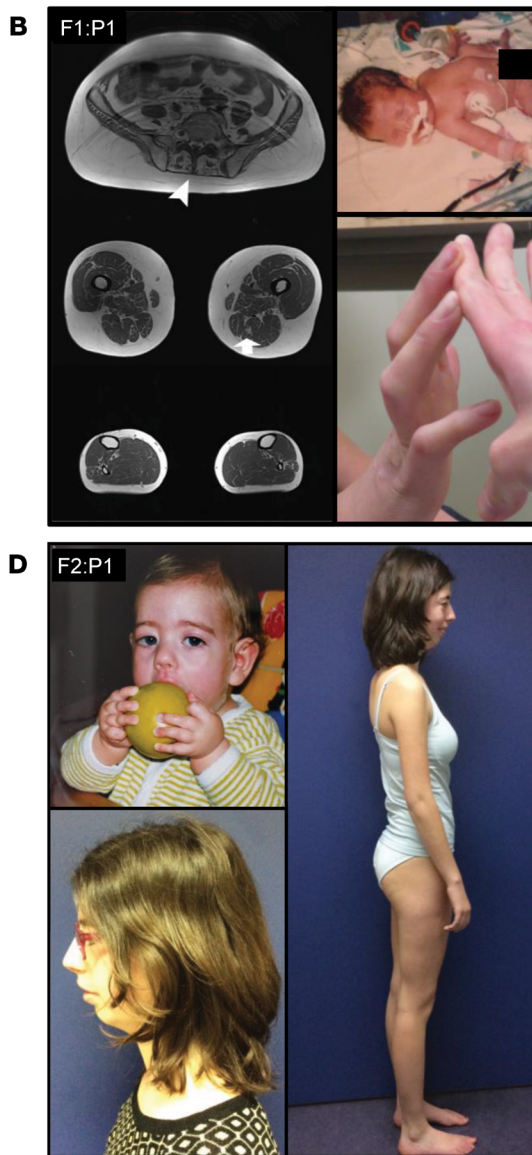
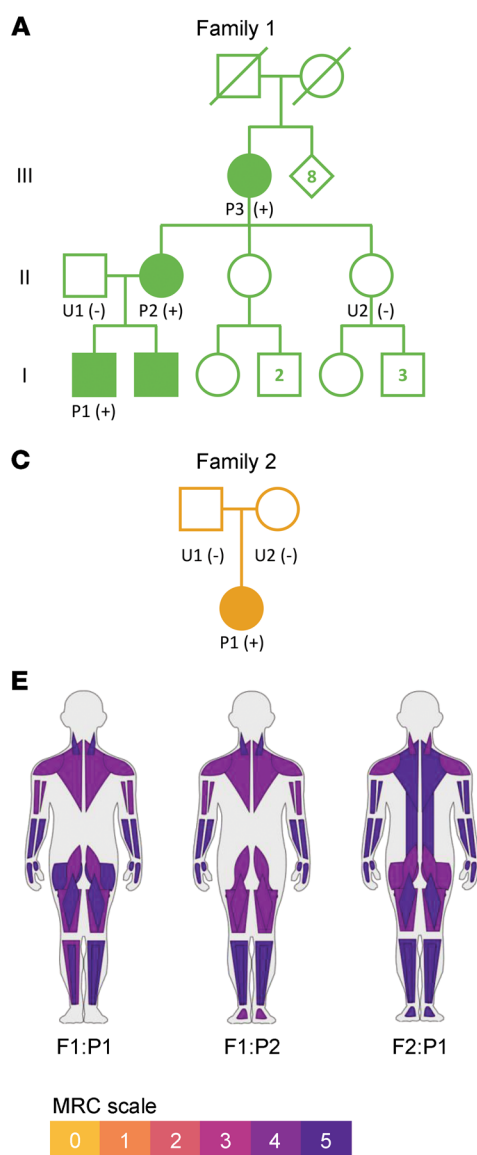
Family/Patient	Clinical phenotype			
	F1:P1	F1:P2	F1:P3	F2:P1
Ethnicity	Caucasian	Caucasian	Caucasian	Caucasian
Sex/age at last examination (yrs)	M/26	F/55	F/76	F/19
TNNC2 mutation	c.100G>T; p.Asp34Tyr	c.100G>T; p.Asp34Tyr	c.100G>T; p.Asp34Tyr	c.237G>C; p.Met79Ile
Inheritance	Dominant	Dominant	Presumed de novo	De novo
Onset	Maternal polyhydramnios treated with serial amniocenteses; hypotonia, vocal cord paralysis, respiratory insufficiency requiring intubation and tracheostomy at birth; PEG tube to address gastroesophageal reflux concerns; camptodactyly with contractures bilaterally and small right ear canal.	Respiratory failure due to stridor and vocal cord paralysis requiring intubation and tracheostomy at birth; scoliosis by 8 days.	Breech presentation; difficulties breathing at birth.	Maternal polyhydramnios treated with serial amniocenteses; reduced fetal movements; severe hypotonia; respiratory weakness; difficulties swallowing requiring PEG tube at 4 mo.
Motor development	Delayed; rolled 10 mo, walked independently 17 mo; difficulties keeping up with peers.	Delayed; sat unsupported 8 mo; rolled 1 yr, walk with support 15 mo; never able to run; difficulty keeping up with peers.	Delayed; walked independently 15 mo; climb stairs and jump 6 yrs; never able to run.	Standing age 1 yr, walked independently age 1.5 yrs. Difficulty keeping up with peers; frequent falls. Unable to run.
Muscle weakness	Improved over time; axial, proximal and distal weakness 4/5 to 5/5 range (MRC grade) (26 yrs); progressive scoliosis requiring spinal fusion surgery with rod placement (16 yrs).	Stable with gradual decline recently; axial, proximal and distal weakness 4/5 to 5/5 range (55 yrs) (MRC grade); mild scoliosis.	Stable with gradual decline recently; mildly reduced 4/5 to 5/5 range (76 yrs) (MRC grade); scoliosis requiring surgery with bone fusions.	Mild proximal weakness 4/5 (MRC grade).
Gait	Waddling gait, unable to get up from a squatting position.	Waddling gait.	Kyphotic posture.	Normal gait, unable to walk on heels or toes. Difficulties with stairs.
Facial involvement	Mild upper and lower facial weakness; ptosis and ophthalmoplegia (childhood).	Mild upper and lower facial weakness; progressive ptosis and ophthalmoplegia (childhood).	Facial weakness, ophthalmoplegia, no ptosis.	Facial weakness; diplopia lateroflexion to the left, increases with fatigue.
Respiratory involvement (age)	FVC 45% predicted (26 yrs).	FVC 73% predicted; 11% decline from sitting to supine (55 yrs).	Tracheoesophageal fistula with pneumonias (74 yrs); FVC 47% predicted (76 yrs).	Recurrent pneumonias until age 3 yrs. FVC 76% predicted (19 yrs).
Cardiac involvement (age)	Echocardiogram normal (26 yrs).	Echocardiogram normal (55 yrs).	Moderate tricuspid regurgitation and trivial pericardial effusion (76 yrs).	Normal electrocardiogram (19 yrs).
Cognitive involvement	Learning disability, graduated high school.	Mild learning disability, graduated high school.		Normal.
EMG/Rep stim (age)	Chronic myopathic process/normal.	NP	NP	NP
Histology (age, muscle biopsied)	Mild variation in fiber size with mild fiber type 2 atrophy; No ultrastructural abnormalities on EM (16 yrs, spinal accessory muscle).	NP	NP	Increase in type 1 fibers, small type 2 fibers. No ultrastructural abnormalities on EM (8 yrs, quadriceps).
LE MRI imaging (age)	Mild, focal fatty infiltration of lower extremity muscles in a patchy and heterogeneous pattern. Paraspinal muscles significantly affected; proximal thigh muscles less affected than lower leg muscles (26 yrs).	Mild, focal fatty infiltration of lower extremity muscles in a patchy and heterogeneous pattern. Proximal thigh muscles less affected than lower leg muscles (55 yrs).	Mild, focal fatty infiltration of lower extremity muscles in a patchy and heterogeneous pattern. Paraspinal muscles significantly affected; proximal thigh muscles less affected than lower leg muscles (76 yrs).	Normal (19 yrs).
Other	Long-standing history of poor appetite and difficulty gaining weight; osteopenia (5 yrs).	Generalized pain; osteopenia (5 yrs).	Osteopenia with 6 bone fractures.	Generalized hypermobility (Beighton 6/9).

F1:P1 indicates patient 1 from family 1, etc. M, male; F, female; yrs, years; mo, months; PEG, percutaneous endoscopic gastrostomy; CK, creatine kinase; EMG, electromyography; Rep Stim, repetitive stimulation; FVC, forced vital capacity; NP, not performed; LE, lower extremity; MRI, magnetic resonance imaging; EM, electron microscopy.

sequencing in P1, P2, and P3, and was absent in the unaffected family member. Thus, in family 1 (F1) the *TNNC2* variant perfectly segregated with disease. WES in F2 (P1) identified a heterozygous de novo variant in *TNNC2*: c.237G>C; p.(Met79Ile); hereafter referred to as M79I. The variant was absent in both parents.

Conservation and location of the mutated TnC residues

gnomAD (<https://gnomad.broadinstitute.org/>) lists 71 rare missense variants in *TNNC2*, compared with the expected occurrence of 106, corresponding to a *z* score of 1.2. This lower-than-expected frequency of missense variants, with a positive *z* score, indicates



increased intolerance of *TNNC2* to heterozygous variation. In general, the amino acid sequence of fsTnC is highly conserved across species (for example, 99% conservation between humans and mice). The mutated residues are conserved across all species queried (Figure 1D). The location of both variants is indicated in Figure 1, C and D, and in the protein 3D structure (see below) of human fsTnC. The missense variant in F1, D34Y, is located in calcium-binding site I where aspartic acid is replaced by a tyrosine residue (Figure 1, C and D). Aspartic acid carries a hydrophilic acidic group with a negative charge. The replacing amino acid, tyrosine, does not carry a charge. The missense variant in F2, M79I, is located in an α -helix next to calcium-binding site II where methionine is replaced by isoleucine, both neutral (Figure 1, C and D).

Muscle (ultra)structure

Structure. From P1 of F1 (F1:P1) and P1 of F2 (F2:P1), muscle biopsies were obtained and used for analyses of muscle (ultra)structure. Hematoxylin and eosin-stained (H&E-stained) sections showed

a slight variation in myofiber size in both patients (Figure 3, A and B). There was no evidence of necrosis, degeneration, inflammation, or fibrosis. Immunohistochemical staining for dystrophin glycoprotein-associated proteins was normal (images not shown). No nemaline rods or inclusions were observed in Gömöri trichrome-stained sections of both patients (Figure 3, C and D). NADH-stained sections showed occasional, scattered atrophic fast-twitch myofibers (Figure 3, E and F). Analysis of myofiber size (minFeret) in both patients showed hypertrophy of slow-twitch myofibers and normally sized fast-twitch myofibers compared with control subjects (Figure 3G and Table 2; note that basic demographic information of the control subjects is shown in Table 3). The proportion of slow-twitch fibers was slightly higher in F1:P1 compared with controls. Fiber type proportion in F2:P1 was comparable to controls (Figure 3H and Table 2).

Ultrastructure. Electron microscopy (EM) showed preserved, intact myofibrillar ultrastructure in myofibers of both patients (Figure 3, I and J). To study the structure of the thin filaments in the myofibrils, we performed experiments at the Advanced Photon

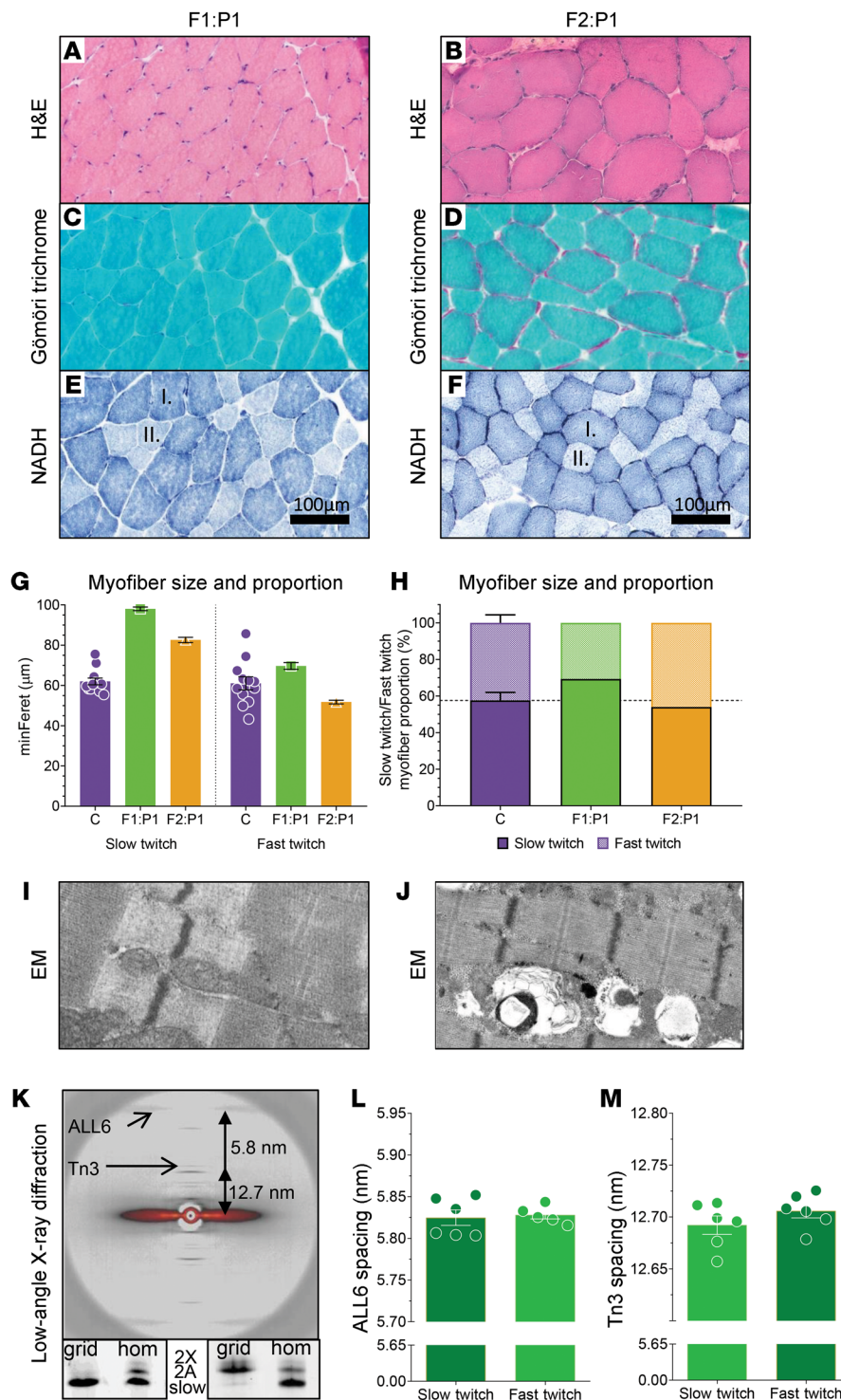


Figure 3. Histology of F1:P1 spinal accessory muscle biopsy at age 16 years (left) and F2:P1 vastus lateralis muscle biopsy at age 9 years (right). (A and B) H&E staining shows mild myofiber size variability in both patients. **(C and D)** Gömöri trichrome staining shows no signs of nemaline rods in myofibers of both patients. **(E and F)** Staining of NADH in muscle cross sections shows larger slow-twitch fibers (dark blue, indicated with "I.") than fast-twitch fibers (light blue, indicated with "II.") in both patients. **(G)** Graph showing the myofiber min-Feret of slow-twitch versus fast-twitch myofibers in control subjects (C), F1:P1, and F2:P1. **(H)** Graph showing the proportion of slow-twitch versus fast-twitch myofibers in control subjects (C), F1:P1, and F2:P1. The dark shading indicates the proportion of slow-twitch fibers and the light shading indicates the proportion of fast-twitch fibers. **(I and J)** Electron microscopy images show no abnormalities, and an intact myofibrillar structure in both patients. **(K)** Top: Typical example of a low-angle x-ray diffraction pattern obtained from 28 fast-twitch myofibers of F1:P1 mounted and aligned in 1 plane between 2 halves of an electron microscopy grid. Note the well-resolved equatorial and meridional reflections. Arrows indicate the actin layer line 6 (ALL6) and Tn3 reflections. Bottom: Myosin heavy chain isoform composition of the myofibers in the grids, showing successful segregation of fast- and slow-twitch fibers from F1:P1 (grid = protein content of F1:P1 grids; hom = muscle homogenate from human diaphragm muscle; 2X and 2A = fast-twitch myosin heavy chain isoforms; slow = slow-twitch myosin heavy chain isoform). Spacing of the ALL6 reflection (**L**) and the Tn3 reflection (**M**) are comparable between slow- and fast-twitch myofibers. Each symbol represents data from 1 set of grids containing 28 myofibers. Data are depicted as mean \pm SEM.

Source (Argonne National Laboratory). Low-angle x-ray diffraction patterns were obtained from preparations in which 28 myofibers were mounted and aligned in a single plane between 2 halves of EM grids (methods described in De Winter et al. [ref. 4]; schematic in Supplemental Figure 1). This approach allowed for high-quality meridional diffraction patterns in relaxed muscle fibers (for example, see Figure 3K). Because *TNNC2* is expressed in fast-twitch myofibers only, we aimed at comparing fast-twitch and slow-twitch fibers within a muscle biopsy of a patient. This approach was only

feasible in F1:P1, as in this biopsy we could segregate fiber types based on visual inspection and produce grids with only slow-twitch myofibers and grids with only fast-twitch myofibers (Figure 3K). The actin layer line 6, indicating the left-handed pitch of the thin filament helix, and the Tn3 reflection, representing the spacing of Tn complexes on the thin filament, were comparable between fast- and slow-twitch fibers (Figure 3, L and M). Thus, the low-angle x-ray diffraction studies suggest that the D34Y variant in *TNNC2* does not affect the structure of the thin filament in fast-twitch myofibers.

Table 2. Myofiber morphology, quantified from histology images

Subject		Myofiber morphology									
		C	(N/n)	F1:P1	(N/n)	%	P value	F2:P1	(N/n)	%	P value
minFeret diameter slow-twitch fibers	μm	60.0 ± 0.6	(12/192)	97.5 ± 1.1	(1/282)	163%	0.001	81.9 ± 1.4	(1/125)	137%	0.023
minFeret diameter fast-twitch fibers	μm	49.3 ± 0.9	(12/110)	66.6 ± 1.4	(1/125)	135%	0.193	51.7 ± 0.9	(1/108)	105%	0.348
Proportion slow-twitch fibers	%	57.6 ± 4.4	(12/192)	69.3	(1/282)	12%	N/A	53.6	(1/125)	-4%	N/A
Proportion fast-twitch fibers	%	42.4 ± 4.4	(12/110)	30.7	(1/125)	-12%	N/A	46.4	(1/108)	4%	N/A

Data are depicted as mean ± SEM. Numbers in bold text indicate statistically significant P values.

MD simulations

To study the effects of the variants in *TNNC2* on the structure and dynamics of fsTnC proteins, we performed 18-μs MD simulations. Simulations were performed for human fsTnC. In our analyses, we focused on the N-terminal domains of fsTnC, as these are critical for thin filament activation during excitation-contraction coupling in skeletal muscle. In short, TnC binds Ca²⁺ at sites I and II in its N-terminal domain (Figure 1C and Figure 4B). Site I is a Ca²⁺-binding loop (or EF-hand) formed by residues 27–37 and site II is a Ca²⁺-binding loop formed by residues 64–74. During Ca²⁺ binding, the loops undergo a conformational change to coordinate Ca²⁺, which then promotes the opening of a hydrophobic pocket on the TnC solvent-exposed surface. This open structure is accompanied by higher mobility in residues 45–55, which correspond to regions in helices B and C that accommodate binding of the TnI switch peptide. Binding of the TnI switch peptide results in downstream conformational changes in the thin filament that ultimately facilitate the binding of myosin to actin (5–7). Figure 4, A and B show the MD-predicted structure of the N-domains of WT and mutated fsTnC, in both the apo (no Ca²⁺ bound) and holo state (Ca²⁺ bound).

Root mean squared fluctuations. First, we assessed the structural dynamics for each amino acid of WT-, D34Y-, and M79I-fsTnC via root mean squared fluctuations (RMSFs). In Figure 4, C and D, the RMSFs are restricted to the N-terminal domain, which isolates the effects of Ca²⁺ binding on the mobility of the domain's helices. In the apo state, WT-fsTnC had high RMSFs in the Ca²⁺-binding loops, which were significantly reduced upon Ca²⁺ binding (holo state). Thus, Ca²⁺ binding stabilized the loops. While a similar reduction in RMSF upon Ca²⁺ binding was observed in the CD loops (which consist of site II formed by α-helices C and D) of D34Y-fsTnC, the D34Y variant rendered the AB loops (which consist of site I formed by α-helices A and B) more mobile in the holo state relative to the apo state (Figure 4C). The presence of the M79I variant promoted greater mobility of the AB loops in the holo state relative to the apo state (Figure 4D), albeit to a lesser extent than the D34Y variant. The M79I variant greatly increased the mobility of residues 45–55, the region that binds TnI switch peptide. Thus, these MD simulations predict that the D34Y and M79I variants in fsTnC perturb the dynamics of regions important for Ca²⁺ binding, while the M79I variant affects the binding of the TnI switch peptide in addition.

Ca²⁺ coordination in holo structures. The binding of Ca²⁺ to EF-hands is determined to a large extent by the number and position of oxygen residues in the Ca²⁺-binding loop (8, 9). We therefore examined the spatial arrangement of the oxygens that bind Ca²⁺ in the AB and CD loops. Both loops exhibit maxima in the radial distribution functions (RDFs) at approximately 2.3 Å (Figure 4, E and G). In the AB loop, the D34Y variant reduces the number of coordinating oxygens (2.5 vs. 6, respectively; Figure 4E), which likely causes the greater mobility in this region, as measured by RMSF. The M79I variant caused a negligible reduction in coordinating oxygens (Figure 4E). Both variants resulted in fewer water molecules leaving the Ca²⁺ coordination shells relative to WT (Figure 4F), which is indicative of a decreased ability of the protein to desolvate the ion. The changes in coordination structure, in particular those caused by the D34Y variant, are likely to impact the thermodynamics of Ca²⁺ binding to the first EF-hand.

Structure and dynamics of the fsTnC hydrophobic pocket. The simulation data suggest that the variants affect the region spanning residues 45–55 (B/C helices). This region is displaced during Ca²⁺ binding to open a hydrophobic pocket that can subsequently bind the TnI switch peptide (10). To quantify these effects, we used principal component analysis (PCA). Two principal components (PCs) account for greater than 60% of the variance, or conformation changes, in our simulated structures (Figure 4I). PC1 captures the displacement of helices B and C (see per-residue contribution to PC1 in Figure 4J), which drives the opening of the hydrophobic pocket following binding of Ca²⁺ to the EF-hands. To a lesser extent, PC1 captures the rearrangement of the Ca²⁺-binding loops in the holo state. Upon projection of the simulation data

Table 3. Basic information on control subjects, F1:P1, and F2:P1

Biopsy	Patient ID	Mutation	Sex	Basic clinical information		Height (cm)	Weight (kg)	BMI
				Age at last investigation (yrs)	Age at biopsy (yrs)			
Control	1	N/A	Male	N/A	44	177	83	26.64
Control	2	N/A	Male	N/A	50	192	117.7	32.1
Control	3	N/A	Male	N/A	50	180	83	25.76
Control	4	N/A	Female	N/A	65	166	66.5	24.13
Control	5	N/A	Female	N/A	53	174	64	21.14
Control	6	N/A	Female	N/A	51	171	68	23.26
Patient	F1:P1	D34Y	Male	26	16	N/A	N/A	N/A
Patient	F2:P1	M79I	Female	21	19	N/A	N/A	N/A

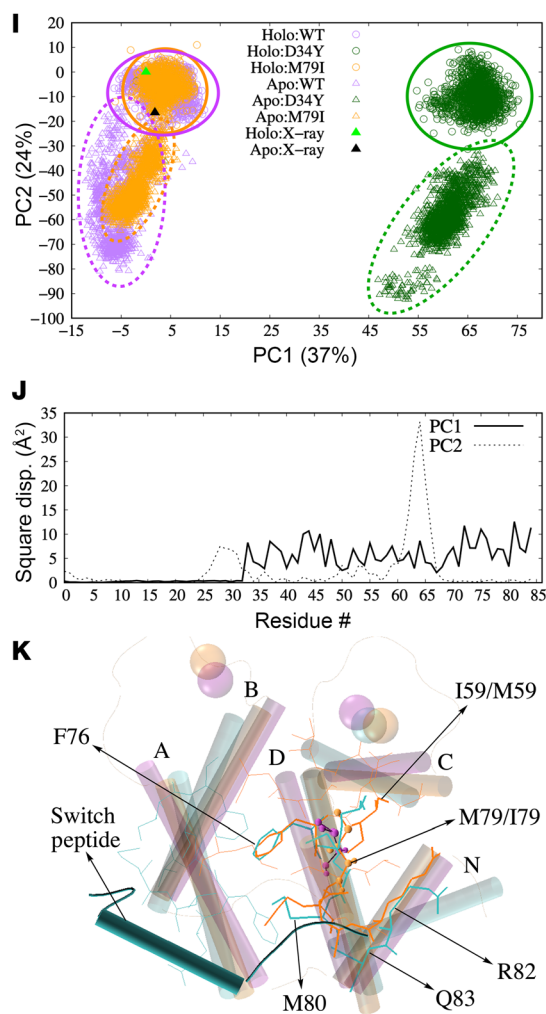
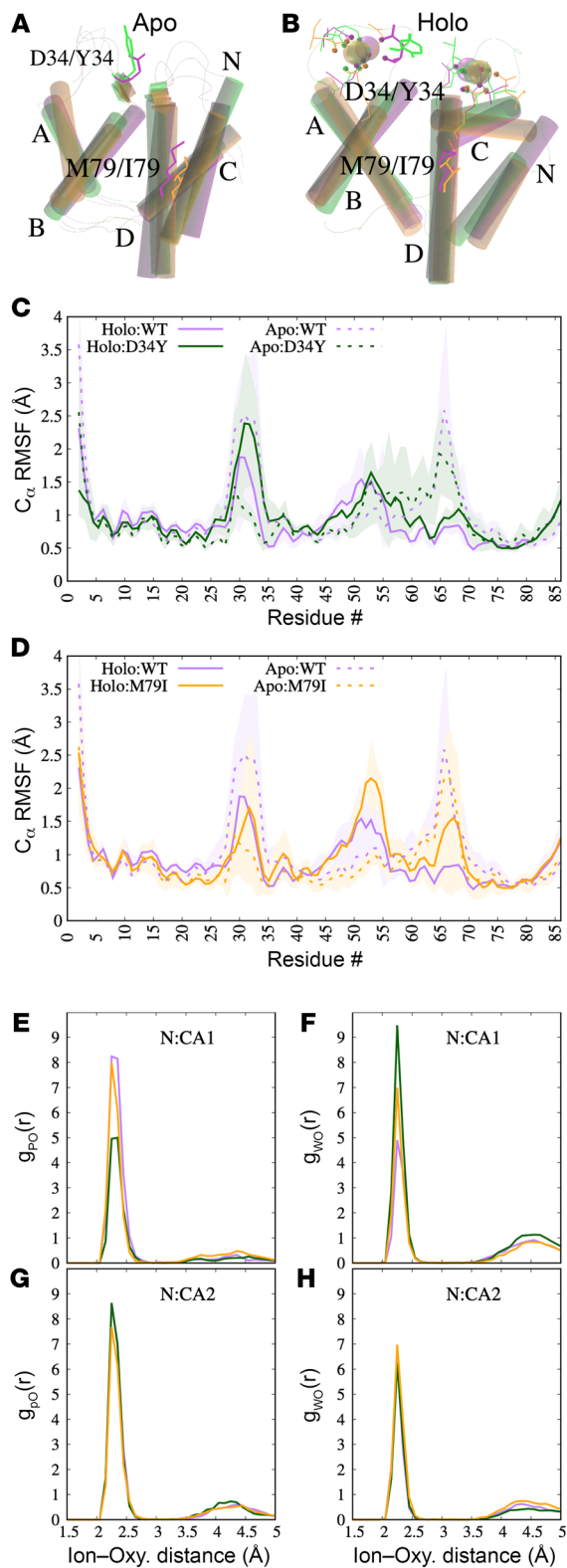


Figure 4. Results of the molecular dynamics simulations. (A and B) Superposition of N-domains of MD-predicted apo (A) and holo (B) variants. WT, D34Y, and M79I variants are colored purple, green, and orange, respectively. Helices N (residues 2–11), A (residues 14–27), B (residues 40–48), C (residues 54–63), and D (residues 74–85) of the N-domain are labeled. Protein oxygens within 2.5 Å of Ca^{2+} are shown as spheres and their respective residues as sticks. (C and D) Root mean squared fluctuations (RMSFs) of N-terminal domain residues. Holo and apo systems are represented as lines and broken lines, respectively. WT is compared against D34Y and M79I in C and D, respectively. Shaded regions reflect standard deviations. (E–H) Radial distribution of protein (E and G) and solvent (F and H) oxygens around bound Ca^{2+} ions in the fsTnC N-terminal domains from the final 50 ns of each trajectory. $g_{\text{PO}}(r)$ and $g_{\text{WO}}(r)$ are the radial distribution functions of the protein and water oxygen atoms around the bound calcium, respectively. N:CA1, N-terminal calcium-binding pocket 1; N:CA2, N-terminal calcium-binding pocket 2. (I and J) Principal component (PC) analysis of the fsTnC2 N-domain MD trajectory data (J). Square displacements signify the relative contribution of each amino acid to PC1 (solid) or PC2 (dashed). PC1 reflects the displacement of helices B–D, while PC2 corresponds to the loop connecting the C and D helices. These PCs demonstrate that the apo structures exhibit different displacements, or conformations, than the holo structures, and the D34Y variant samples a very different conformation than the WT and the M79I variants. (K) Cartoon diagram of the MD-predicted structures for holo WT-fsTnC (purple), holo M79I-fsTnC (orange), and holo cTnC with switch peptide (cyan). The structures of WT- and M79I-fsTnC are from the MD simulations; for cTnC the PDB 1MXL structure was used. Residues that are within 4 Å of the TnI switch peptide in cTnC are shown as cyan sticks, and residues within 4 Å of M79/I79 in holo M79I-fsTnC are shown as orange sticks. Residues that overlap between the 2 are shown as thick sticks. M79/I79 is shown in ball and stick representation.

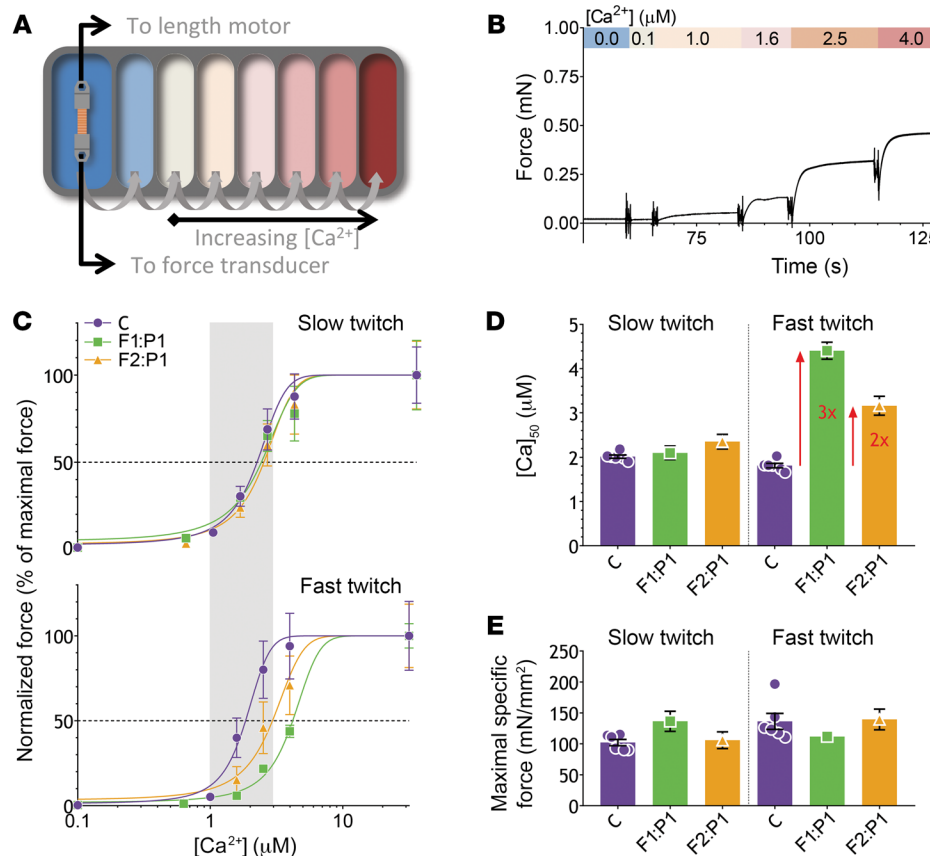


Figure 5. The experimental design and results of the myofiber contractility experiments. (A) Schematic representation of the contractility setup. An isolated single myofiber between aluminum T-clips is mounted between a force transducer and length motor. The fiber is subsequently passed through the baths filled with solutions with increasing $[Ca^{2+}]$. (B) Typical tracing showing the force response to the increasing $[Ca^{2+}]$, followed by the protocol in which a rapid release and restretch (k_{TR}) and short-length perturbations (active stiffness) were imposed on the myofibers ($[Ca^{2+}]$, k_{TR} , and active stiffness are indicated in the colored bar). Data shown are from a control myofiber (fast twitch, CSA = 0.0054 mm 2). (C) The force– $[Ca^{2+}]$ relationship, showing the average of all slow-twitch (top) and fast-twitch (bottom) control myofibers (C) versus the slow-twitch and fast-twitch myofibers from F1:P1 and F2:P1. The physiological $[Ca^{2+}]$ range is indicated by the gray bar. (D) The $[Ca^{2+}]$ at which 50% of maximal force is reached. (E) The maximal force normalized to myofiber CSA (i.e., specific force). Data are depicted as mean \pm SEM.

into the PC1 basis, the WT apo state assumes more negative values, while its holo state yields more positive values (Figure 4I). In other words, the WT holo state generally features a more open hydrophobic pocket than the apo state. The PC1 projections for both apo and holo states of D34Y-fsTnC are markedly different from those for WT-fsTnC (Figure 4I). This is likely a consequence of both the AB loop and the helices B/C being perturbed relative to the WT. We speculate that these effects of D34Y impede the exposure of the hydrophobic pocket, which is necessary for binding the TnI switch peptide.

The projections for the M79I-fsTnC apo and holo states are comparable to that of WT-fsTnC. PC2, which describes the contraction of the AB and CD loops upon Ca^{2+} binding (Figure 4J), shows no major effect of the variants (Figure 4I).

Effects beyond the coordination regions and the hydrophobic pocket. Figure 4D shows that the M79I variant enhanced the mobility of the B/C helices, but this did not manifest in significant structural changes relative to WT based on our PC analysis. We therefore examined whether the substitution of the isoleucine at position 79 induces subtle changes in the hydrophobic patch that could impinge on the binding of the TnI switch peptide. We used the cardiac TnC-TnI complex (PDB: 1MLX) to approximate the binding pose of the TnI switch peptide in fsTnC. Figure 4K shows the cTnC-TnI complex superimposed onto fsTnC. The cardiac TnI position is accommodated into the fsTnC hydrophobic pocket without introducing unfavorable steric overlap between the proteins. The isoleucine side chain does not present any steric overlaps with the cTnI peptide. However,

among the amino acids that are directly adjacent to both TnI and the M79 position, I59, F76, M80, R82, and Q83 are displaced by roughly 2 Å. Thus, the M79I variant appears to reorganize the hydrophobic patch configuration.

In an effort to test the hypothesis that the M79I variant perturbs the TnC and TnI interaction, we simulated an intact Tn complex comprising TnC, TnI, and TnT. For this purpose we simulated via all-atom MD (Supplemental Figure 2A) the holo forms of the WT and M79I variants, based on structural data for the human cardiac Tn complex (PDB: 1J1E), as analogous structural data for the skeletal muscle isoforms have not been reported (11). The MD data suggest that the M79I variant perturbs the TnI interaction with the N-domain of TnC. This is evident as a displacement of the interacting TnI peptide in the presence of the M79I variant relative to its position in the presence of the WT (Supplemental Figure 2B). Our data indicate that this displacement may be due to the pathogenic variant forming a new contact between TnC-I79 and TnI-M155 that is not evident in WT-TnC. This difference may arise from an alternate side chain placement of TnI-V148 (Supplemental Figure 2B). Although structural data are not available to validate this prediction, the finding of a displaced TnI inhibitory peptide for the M79I variant is consistent with our hypothesis that M79I alters TnI-TnC interactions.

Thus, altogether, the MD simulations suggest that the D34Y variant has the most significant impact on the fsTnC structure, by affecting the displacement of the first N-terminal EF-hand following Ca^{2+} binding, the coordination of Ca^{2+} binding by oxygens, and impeding the exposure of the hydrophobic pocket, to which

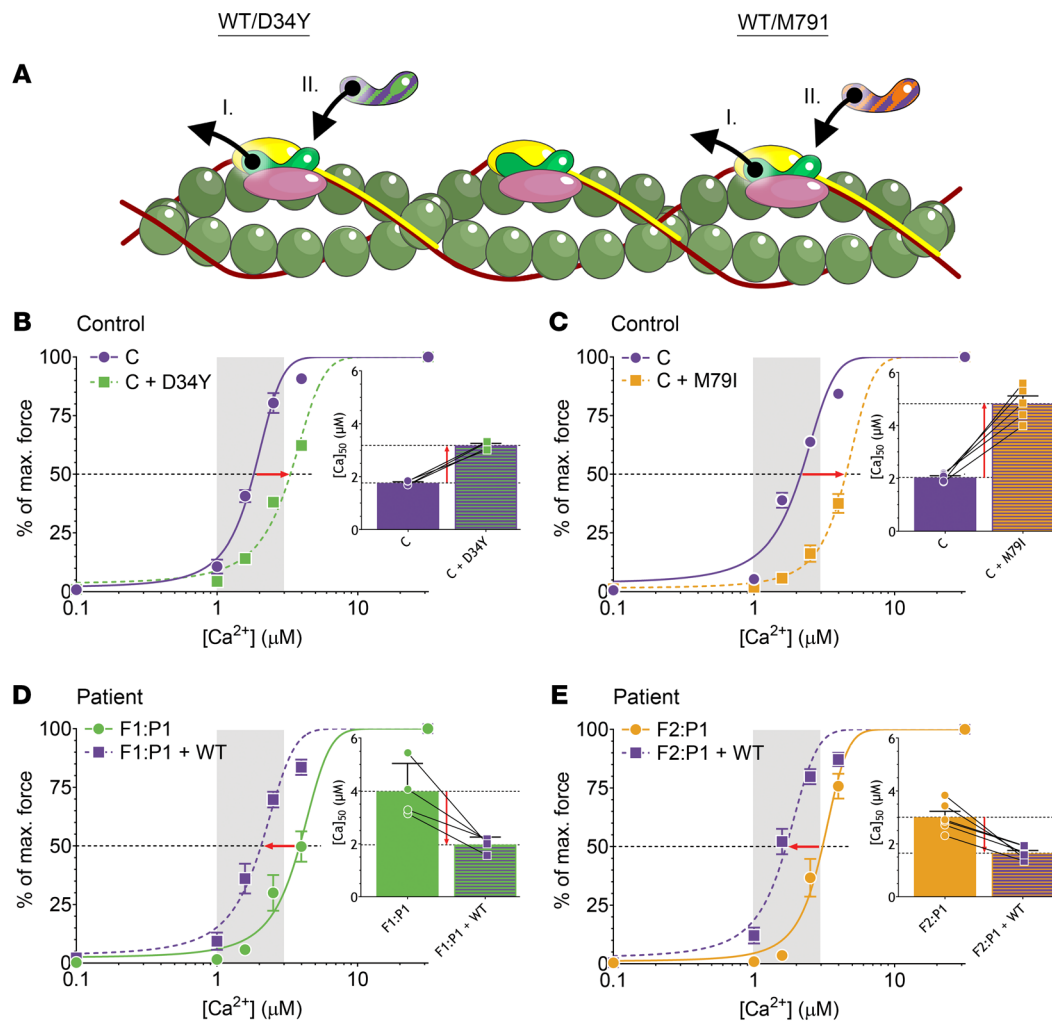


Figure 6. The experimental design and results of the reconstitution of myofibers with recombinant fsTnC. (A) The schematic depicts the thin filament with troponin complex in which (I) endogenous fsTnC is removed from fast-twitch myofibers, followed by (II) reconstitution with exogenous fsTnC. (B and C) Normalized force-[Ca²⁺] relationships of myofibers from control subjects before and after reconstitution with recombinant D34Y-fsTnC (B) and M791-fsTnC (C). Insets show the [Ca²⁺] at which 50% of maximal force is reached. (D and E) Normalized force-[Ca²⁺] relationships of myofibers from F1:P1 (D) and F2:P1 (E) before and after reconstitution with recombinant WT-fsTnC. Insets show the [Ca²⁺] at which 50% of maximal force is reached. The physiological [Ca²⁺] range is indicated by the vertical gray bar. Data are depicted as mean \pm SEM.

the TnI switch peptide binds. The M791 variant has more modest effects that manifest in greater mobility of the fsTnC B/C helices following Ca²⁺ binding and may interfere with the fsTnC-fsTnI switch peptide interface. These effects of the *TNNC2* variants on the structure and dynamics of fsTnC might impact the calcium sensitivity of force generation of sarcomeres.

Myofiber contractility

Force production and calcium sensitivity. To study whether the structural changes in mutated fsTnC impair the contractility of sarcomeres, we isolated myofibers from the patients' biopsies using microforceps. Myofibers were permeabilized, exposed to increasing [Ca²⁺] solutions, and the force generated was recorded (Figure 5, A and B). To account for differences in myofiber size, absolute maximal force was normalized to the cross-sectional area (CSA) of the myofiber to obtain specific force. In both patients, the maximal specific force of slow-twitch and fast-twitch myofibers

was comparable to that of myofibers from control subjects (Figure 5E). Thus, these findings indicate the *TNNC2* variants do not affect the maximal force-generating capacity of the sarcomeres.

In Figure 5C, the force-[Ca²⁺] relationships are shown for slow-twitch and fast-twitch myofibers of control subjects, F1:P1, and F2:P1. Slow-twitch myofibers show no differences in the force-[Ca²⁺] relationship between groups. However, in fast-twitch myofibers of F1:P1 and F2:P1, the force-[Ca²⁺] relationship is markedly shifted rightwards, indicating a lower Ca²⁺ sensitivity of force. The rightward shift of the force-[Ca²⁺] relationship is illustrated by the higher [Ca₅₀]^Δ, i.e., the [Ca²⁺] at which 50% of maximal force is produced (F1:P1: Δ = +2.59 μM, *P* < 0.001; F2:P1: Δ = +1.35 μM, *P* < 0.001). This indicates that in patients' myofibers more Ca²⁺ is required to generate 50% of maximal force production (Figure 5D).

Thus, the major phenotype of the myofibers of the patients with *TNNC2* variants is a markedly reduced calcium sensitivity of force in fast-twitch myofibers.

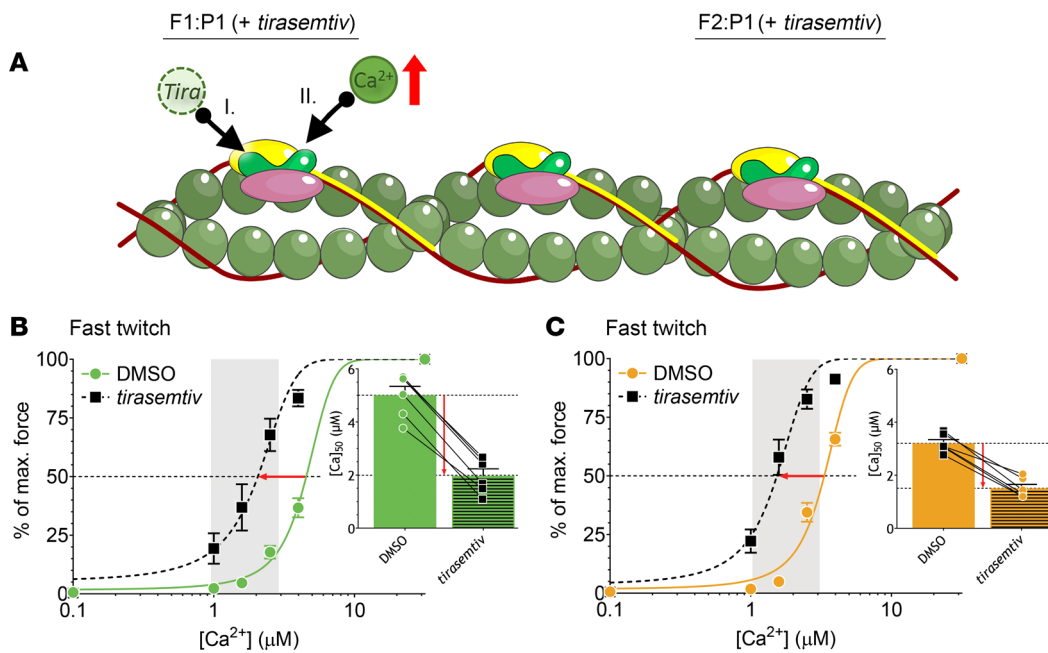


Figure 7. Experimental design and results for myofibers of controls (C), F1:P1, and F2:P2 exposed to DMSO and tirasemtiv. (A) Schematic depiction of a thin filament section including 1 troponin subunit illustrating the Ca^{2+} -sensitizing effect of tirasemtiv: tirasemtiv is added to the pCa solution (I), enhancing Ca^{2+} binding to troponin in fast-twitch myofibers (II). (B and C) Normalized force- $[\text{Ca}^{2+}]$ relationships of fast-twitch myofibers of F1:P1 (B) and F2:P1 (C) before and during exposure to 10 μM tirasemtiv. Insets show the $[\text{Ca}^{2+}]$ at which 50% of maximal force is reached. The physiological $[\text{Ca}^{2+}]$ range is indicated by the vertical gray bar. Data are depicted as mean \pm SEM.

Reconstitution of myofibers with fsTnC

To study whether the reduced calcium sensitivity of force in patients' myofibers is a direct cause of the presence of mutant fsTnC in the sarcomeres, we studied whether replacing the endogenous, mutant fsTnC with recombinant, WT-fsTnC would restore the contractile function of patients' myofibers. In brief, permeabilized fast-twitch myofibers were exposed to an extraction solution, removing endogenous fsTnC. Thereafter, recombinant fsTnC was introduced into these myofibers (Figure 6A). We did not assess the level of incorporation of mutant proteins, but we did measure the maximal force production of myofibers before extraction (baseline force), after extraction of endogenous fsTnC, and after reconstitution with exogenous fsTnC. Successful extraction of endogenous fsTnC from the myofibers of control subjects and patients was assumed based on the reduced maximal force generation of extracted myofibers (Supplemental Table 1), and successful reconstitution with endogenous fsTnC was indicated by the restoration of maximal force (Supplemental Table 1). Thus, the stage was set to test the effect of the TNNC2 variants on the force- $[\text{Ca}^{2+}]$ relationship in myofibers.

Before extraction and after reconstitution of the myofibers with recombinant fsTnC, the force- $[\text{Ca}^{2+}]$ relationship was determined (Figure 6, B-E) to assess the calcium sensitivity of force generation. Reconstitution of myofibers of controls with WT-fsTnC did not affect the calcium sensitivity of force (Supplemental Figure 3 and Supplemental Table 2). This indicates that the protocol used for the extraction and reconstitution had no adverse effects on the contractility of myofibers. Interestingly, reconstitution of myofibers of controls with D34Y-fsTnC or M79I-fsTnC

decreased the calcium sensitivity of force (Figure 6, B and C, respectively; and Supplemental Table 2); after reconstitution with D34Y-fsTnC, 80% more Ca^{2+} was required to generate 50% of maximal force; after reconstitution with M79I-fsTnC, 137% more Ca^{2+} was required (Figure 6, B and C, insets; and Supplemental Table 2). Thus, we could successfully evoke the patients' phenotype in myofibers of healthy controls by replacing endogenous fsTnC with exogenous, mutated fsTnC.

Next, we performed the opposite experiment, i.e., replacing mutant fsTnC in the patients' myofibers with WT-fsTnC. After reconstituting the F1:P1 myofibers with WT-fsTnC, the calcium sensitivity of force was restored to control values (Figure 6D and Supplemental Table 2). This was also observed after reconstituting F2:P1 myofibers with WT-fsTnC (Figure 6E and Supplemental Table 2). We also reconstituted F1:P1 myofibers with a 50:50 mixture of WT- and D34Y-fsTnC and observed an increase in the calcium sensitivity of force (Supplemental Tables 1 and 2), with a $\Delta[\text{Ca}^{2+}]_{50}$ that was approximately 50% of the increase after reconstitution with 100% WT-fsTnC. Reconstitution of F2:P1 myofibers with a 50:50 mixture of WT- and M79I-fsTnC did not increase the calcium sensitivity of force (Supplemental Tables 1 and 2). These findings support the dominant effect of the variants, with the most profound effect elicited by the M79I variant.

Thus, reconstituting healthy human myofibers with D34Y-fsTnC or M79I-fsTnC decreases the calcium sensitivity of force, while reconstituting patient myofibers with WT-fsTnC increases the calcium sensitivity of force back to normal values. These findings indicate that we can mimic the patients' phenotype in control myofibers by reconstitution with D34Y- and M79I-fsTnC, and

repair the calcium sensitivity of force in patients' myofibers by reconstitution with WT-fsTnC. These experiments conclusively establish the pathogenicity of the variants in *TNNC2*.

Effect of tirasemtiv on myofiber contractility

Tirasemtiv was used to study the ability of a fast skeletal muscle Tn activator to repair the contractility of patients' fast-twitch myofibers. In brief, permeabilized fast-twitch myofibers isolated from patients' muscle biopsies were exposed to various Ca^{2+} solutions in the absence and presence of 10 μM tirasemtiv (Figure 7A). This concentration was selected based on previous work from our group (12). In fast-twitch fibers of both F1:P1 and F2:P1, tirasemtiv restored the calcium sensitivity of force to control values (Figure 7, B and C, respectively; and Supplemental Table 3). We also tested the effect of tirasemtiv on slow-twitch myofibers; these data are in the Supplemental Methods. Note that, unexpectedly, tirasemtiv also increased the maximal force of F1:P1 fast-twitch myofibers, and this was also observed in F2:P1, although to a lesser extent; the magnitude of maximal force increase induced by tirasemtiv correlated with the magnitude of the decrease in the $[\text{Ca}^{2+}]_{50}$ of the patient fibers relative to control values (Supplemental Figure 4). Fibers of control subjects showed no increase in maximal force in response to tirasemtiv (Supplemental Figure 4C). Thus, tirasemtiv increased the force generated by patients' myofibers at physiological $[\text{Ca}^{2+}]$ to that generated by control myofibers.

Discussion

This study reports variants in *TNNC2*, the gene encoding fsTnC, as a cause of human disease. Two missense variants were identified in unrelated families (c.100G>T, D34Y; c.237G>C, M79I). Patients from both families presented with a distinct and recognizable phenotype of congenital weakness in combination with severe congenital respiratory insufficiency. This phenotype improved over time, allowing for ambulation and respiratory independence that are atypical for congenital myopathies, which often have a static or progressive nature. Other notable features include facial weakness, ptosis, decreased extraocular movements, and jaw contractures.

We provide strong evidence for pathogenicity of the *TNNC2* variants. Because the calculation of a conclusive LOD (logarithm [base 10] of odds) score of greater than 3.0 was not possible due to the limited number of scorable meioses in family 1, we obtained several layers of additional evidence. As noted, the pedigree analysis in F1 showed perfect segregation of the variant with disease in 3 generations under dominant inheritance and full penetrance, while the patient in F2 has a de novo variant in *TNNC2* (paternity and maternity confirmed) with no family history of muscle disease, compatible with pathogenicity of the variants. Furthermore, during the past years, we have sequenced the exomes of approximately 1400 patients with neuromuscular disease, and never identified patients with variants in *TNNC2*, except the patients presented here. These variants have also never been documented in the 125,000-person gnomAD cohort of normal individuals, consistent with their pathogenicity in the heterozygous state. Also, the clinical phenotype in both families is highly unusual and entirely consistent between the 2 families, who on our analysis only share the *TNNC2* variants and do not have variants in any of the oth-

er established myopathy genes. Finally, we provide experimental functional evidence supporting pathogenicity; MD simulations indicated that the location of the variants affects the structure of the protein product and might impair the force response of myofibers to submaximal Ca^{2+} concentrations, which was confirmed in functional assays in patients' myofibers. Importantly, the contractile phenotype in patients' myofibers was repaired by replacing the mutant fsTnC with recombinant WT-fsTnC (Figure 6, D and E). Conversely, the contractile phenotype was evoked by replacing fsTnC in myofibers from healthy control subjects with recombinant, mutant fsTnC (Figure 6, B and C). According to the variant classification criteria of the American College of Medical Genetics and Genomics (13), these multiple layers of evidence, including experimental functional evidence, classify the *TNNC2* variants as pathogenic (F1: PS3, PM2, PP3; F2: PS2, PS3, PM2, PP3).

Thin filament-associated protein disorders define a subgroup of congenital disorders of muscle, including those associated with variants in TnT (*TNNT1* and *TNNT3*) (14, 15), α -actin 1 (*ACTA1*) (16), α - and β -tropomyosin (*TPM3* and *TPM2*) (17, 18), nebulin (*NEB*) (19), leiomodin-3 (*LMOD3*) (20), cofilin 2 (*CFL2*) (21), unconventional myosin 18B (*MYO18B*) (22), myopalladin (*MYPN*) (23), kelch family members 40 (*KLHL40*) and 41 (*KLHL41*) (24, 25), and kelch repeat and BTB (POZ) domain-containing 13 (*KBTBD13*) (26), but not yet in *TNNC2*. Many of these disorders histologically feature nemaline rods as the defining characteristic of nemaline myopathies, which were notably absent in myofibers of F1:P1 and F2:P1 (Figure 3). We acknowledge, however, that there are many other examples of mutations in nemaline myopathy genes without nemaline rods, and it is entirely possible that there are nemaline rods somewhere in certain muscles/fibers that were however not sampled in the patients studied here. Another remarkable feature of the *TNNC2*-related myopathy described here is the subsequent clinical improvement in strength and respiratory function following the severe postnatal respiratory insufficiency and weakness in all 4 patients. Although some degree of clinical improvement may occur in patients with congenital myopathy, the degree to which the patients with *TNNC2*-related myopathy improved is highly unusual. Thus, variants in *TNNC2* cause a distinct congenital phenotype. The basis of the clinical improvement might relate to the switch from predominantly fast-twitch (*TNNC2*-expressing) myofibers in muscles after birth to a 50:50 distribution of slow- and fast-twitch myofibers at older ages (27). Hence, with age-related muscle maturation, this switch toward more slow-twitch myofibers might help compensate for the initially more pronounced pathogenic effect of the *TNNC2* variants. Human laryngeal myofibers rely on fast isometric contractions for proper respiration and airway protection so that the prominent stridor contributing to the early respiratory failure might be attributable to this (28). It is, however, unclear whether there are postnatal developmental changes in myofiber type composition that make laryngeal muscles less dependent on fsTnC, and thus account for the unusual clinical improvement in respiratory function. Of note, a fast-to-slow fiber type switch does not occur in the extraocular muscles, which continue to be affected in the patients. Slow-twitch myofibers should be able to compensate effectively as they are spared functionally, generating normal force (Table 4), as well as histologically in that we observed a mild hypertrophy of

Table 4. Contractility data of slow- and fast-twitch myofibers of control subjects (C) and F1:P1 and F2:P1

Subject		Slow-twitch myofibers						Fast-twitch myofibers			
		C	(N/n)	F1:P1	(N/n)	%	P value	F2:P1	(N/n)	%	P value
Max. force normalized to CSA	mN/mm ²	102.1 ± 5	(6/39)	136.4 ± 16.2	(1/2)	34%	0.131	105.9 ± 13.5	(1/7)	4%	0.845
[Ca ²⁺] ₅₀	μM	0.00202 ± 0.00004	(6/37)	0.0021 ± 0.00015	(1/2)	4%	0.548	0.00235 ± 0.00016	(1/10)	16%	0.029
<i>n</i> _{Hill}		3.26 ± 0.1	(6/37)	2.39 ± 0.17	(1/2)	-27%	0.330	3.43 ± 0.27	(1/10)	5%	0.872
Subject		Slow-twitch myofibers						Fast-twitch myofibers			
		C	(N/n)	F1:P1	(N/n)	%	P value	F2:P1	(N/n)	%	P value
Max. force normalized to CSA	mN/mm ²	136.3 ± 12.9	(6/31)	111.9 ± 7.9	(1/16)	-18%	0.332	139.5 ± 16.7	(1/10)	2%	0.350
[Ca ²⁺] ₅₀	μM	0.00181 ± 0.00005	(6/39)	0.0044 ± 0.00019	(1/16)	143%	0.000	0.00316 ± 0.00021	(1/12)	75%	0.000
<i>n</i> _{Hill}		4.43 ± 0.36	(6/39)	2.63 ± 0.07	(1/16)	-41%	0.029	3.23 ± 0.22	(1/12)	-27%	0.086

All data are depicted as mean ± SEM. The number of measured biopsies (N) and single myofibers (*n*) is shown, as well as the percentage change of patients compared with control and the P value. *n*_{Hill} = Hill coefficient.

slow-twitch myofibers (Figure 3) and not the slow-twitch myofiber atrophy and predominance that is a feature commonly seen in the nemaline myopathies (3). Furthermore, during daily life activities, the affected fast-twitch myofibers are recruited to a much lesser degree than the spared slow-twitch myofibers (Henneman's size principle). Consequently, the relatively low activity level of fast-twitch myofibers might facilitate timely turnover of mutant protein in the myofibers and prevent disease progression. These mechanisms might also underlie the reported improvement with age of the clinical phenotype of patients with mutations in other fast-twitch muscle genes such as *TNNT3* (15, 29).

TNNC2 is highly conserved across species, including the sequence surrounding the variants (Figure 1D). Both variants found in the 2 families act in a heterozygous dominant manner, so that both WT and mutant protein are expected to be expressed in myofibers. Our studies indicate that mutant proteins were incorporated in the thin filaments, as replacing endogenous fsTnC in patients' myofibers with WT recombinant fsTnC completely restored the contractile phenotype (Figure 6). Furthermore, it is unlikely that haploinsufficiency contributed to the contractile phenotype, as that should have compromised the maximal force-generating capacity of the myofibers, which was not observed (Table 4).

In contrast with many other congenital myopathies genes (3), variants in *TNNC2* do not appear to cause muscle weakness by myofiber atrophy (Figure 3G) or by damaged myofibrillar ultrastructure (Figure 3, I–M). Indeed, the maximal force-generating capacity of fast-twitch myofibers isolated from patients' biopsies was similar to those isolated from biopsies of control subjects (Table 4). The findings from the contractility assays in permeabilized myofibers, assays in which possible confounding effects of Ca²⁺ handling by the sarcoplasmic reticulum are absent, revealed that the muscle weakness is primarily caused by a strong reduction in the Ca²⁺ sensitivity of force generation by the sarcomeres (Figure 5). The sarcomeres in fast-twitch myofibers of F1:P1 required 3-fold more Ca²⁺ to generate 50% of maximal force, whereas myofibers of F2:P1 required 2-fold more Ca²⁺. Note that this more pronounced phenotype in F1:P1 at the myofiber level at least partly explains the more severe clinical

phenotype of patients with the D34Y variant compared with the patient with the M79I variant. The pathogenicity of the variants was established in experiments in which the contractile phenotype was evoked by replacing endogenous fsTnC in myofibers from control subjects with recombinant, mutant fsTnC (Figure 6). Conversely, we could repair the contractile phenotype of myofibers from patients by replacing endogenous, mutant fsTnC with recombinant, WT fsTnC (Figure 6). The MD simulations suggested 2 different molecular mechanisms for the D34Y and M79I variants that underlie the reduced Ca²⁺ sensitivity of force. The D34Y variant had the most pronounced effect on fsTnC and might change the displacement of the first N-terminal EF-hand following Ca²⁺ binding and impede the exposure of the hydrophobic pocket to which the TnI switch peptide binds. The MD simulations suggested a more subtle effect from the M79I variant, which might directly impinge on the binding of the TnI switch peptide by displacing residues I59, F76, M80, R82, and Q83 by 2 Å. These residues constitute part of the solvent-exposed hydrophobic patch that interfaces with the TnI switch peptide. Indeed, simulations of the intact Tn complex comprising TnC, TnI, and TnT suggested that the M79I variant perturbs the placement of the TnI switch peptide (Supplemental Figure 2). Since the binding of the TnI switch peptide is a requisite step in force generation that directly follows Ca²⁺ binding in the fsTnC N-terminal domain, it is plausible that the variants considered in this study may interfere with the TnC-TnI interaction. The more pronounced effects of the D34Y variant on fsTnC dynamics, relative to those of M79I, are in line with the larger reduction in the calcium sensitivity of force in F1:P1 relative to F2:P1 (Figure 5). Whether the *TNNC2* variants, and in particular the D34Y variant, impact the binding of Ca²⁺ to fsTnC, as the MD simulations suggest, should be addressed in future studies.

Therapeutic approaches to a *TNNC2*-related myopathy include the competitive introduction of WT-fsTnC in patients' muscles by adeno-associated virus-mediated (AAV-mediated) gene therapy. Recent advances show the potential of AAV vectors in gene therapy for neuromuscular diseases, and AAV vector-mediated gene delivery was recently approved for spinal muscular atrophy (30–32). Our in vitro results suggest that competing

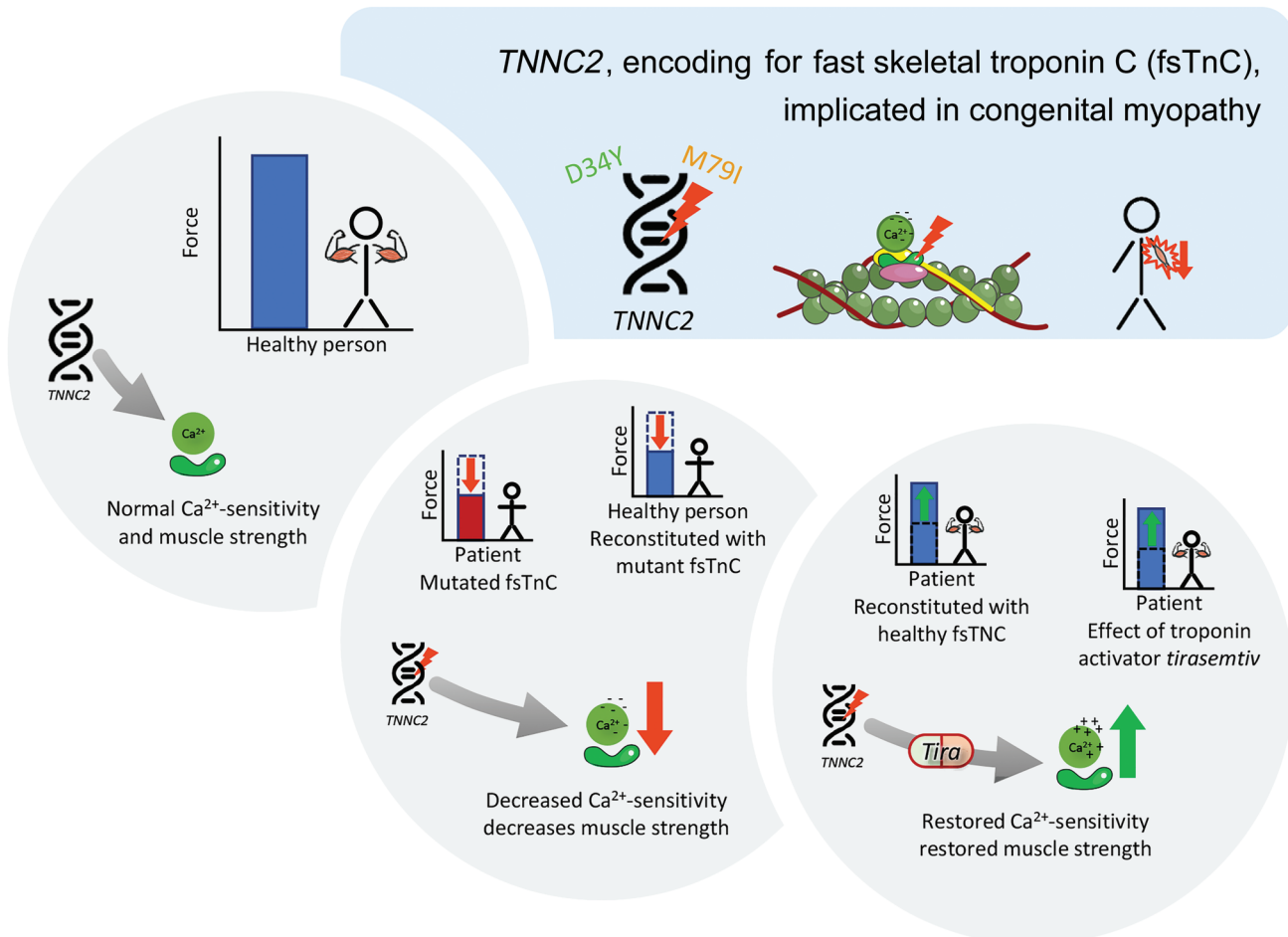


Figure 8. Graphical summary of the pathomechanism in *TNNC2*-related congenital myopathy.

off the mutant fsTnC with WT-fsTnC results in correction of the contractile phenotype. However, targeting WT *TNNC2* to fast-twitch muscle fibers only is one of the challenges that would need to be met. Using a small-molecule strategy to target the physiological consequences of the variant rather than the variant itself, is another potentially valid approach to address this condition. In the present study, we tested the ability of the small molecule fast skeletal muscle Tn activator tirasemtiv to augment the force response to calcium in myofibers of patients. Tirasemtiv binds to fsTnC and amplifies the response of the thin filament to calcium in fast-twitch myofibers, leading to increased muscle force at submaximal rates of nerve stimulation (33). Thus, fast skeletal muscle Tn activation might offer a feasible therapeutic approach in patients with *TNNC2* variants. In our studies we tested the effect of 10 μM tirasemtiv, a concentration we have used in previous work and which elicits a maximal force response without affecting the relaxation kinetics of myofibers (12). Although a relatively high concentration, it is considerably lower than the TnC concentration in skeletal muscle, and, furthermore, tirasemtiv is specific for fsTnC and does not bind elsewhere in the sarcomere to activate muscle (33, 34). Importantly, at physiological calcium concentrations, the force generated by patients' myofibers increased by up to 600% in the presence of tirasemtiv, and reached values that were close to or even higher than those of healthy subjects

(Figure 7). An interesting observation was that tirasemtiv not only increased the force response to submaximal calcium concentrations, but also to saturating calcium concentrations (approximately 40%; Supplemental Figure 3). This effect was not observed in previous studies with tirasemtiv (e.g., Russell et al. [ref. 33] and Hwee et al. [ref. 35]), although Lee et al. (36) showed an approximately 7% increase. We speculate that this effect relates to tirasemtiv binding to the interface of TnC and TnI (33). The *TNNC2* variants induce structural alterations in or near this interface (Figure 4), and might enhance the effect of tirasemtiv on the Ca^{2+} off rates, even at saturating calcium concentration. Although tirasemtiv did not meet its primary endpoint in a recent phase III clinical trial in patients with amyotrophic lateral sclerosis, due in part to tolerability (including dizziness, fatigue, nausea, weight loss, and insomnia) (37), our findings illustrate the great therapeutic promise of fast skeletal muscle Tn activation. Reldesemtiv, a second-generation fast skeletal muscle Tn activator that is structurally distinct from tirasemtiv, has a lower side-effect profile and is currently under clinical trial investigation (38, 39).

In summary, we characterized 2 families with a distinct congenital myopathy caused by dominantly acting variants in *TNNC2*. Recognition of the *TNNC2*-related phenotype reported here may facilitate early diagnosis and management. Furthermore, by combining molecular dynamics simulations and myofiber contractility

studies, we showed that the disease mechanism of *TNNC2*-related myopathy is driven by a reduction in the calcium sensitivity of force (graphic summary in Figure 8), thus providing a potential promising avenue for therapeutic intervention.

Methods

A summary of the methods applied is described below. Additional details are in the supplemental material.

Patient recruitment and sample collection

Patients' and control subjects' general information are in Table 3. A detailed clinical description of both patients' families is in Table 1. Additional details of human study approval, informed consent, and image approval can be found below in the study approval section and further details of recruitment and sample details are in the supplemental material.

Genetic testing

WES was performed on genomic DNA extracted from blood. WES on F1:P1, F1:P2, and F1:P3 was performed through the NIH Intramural Sequencing Center (NISC) using the Nimblegen SeqCap EZ Exome +UTR Library and Illumina HiSeq 2500 sequencing instruments. WES data were analyzed using an exome-based targeted-panel approach (exome slice) to identify variants in known neuromuscular disease genes, with subsequent reflex analysis of all WES-generated data. Pathogenicity was assessed using the American College of Medical Genetics and Genomics/Association for Molecular Pathology guidelines for interpretation of sequence variants, which includes population data, computational and predictive data using various lines of computational evidence (CADD, Polyphen, Sift), and segregation data (13). Variants were also analyzed using Varsifter and searched for in dbSNP and NHLBI EVS (40, 41). The *TNNC2* variant was confirmed by Sanger sequencing in F1:P1, F1:P2, and F1:P3, and in unaffected relatives F1:U1 and F1:U2 using DNA extracted from saliva. DNA from P3's parents was not available for segregation testing. WES on F2:P1 and her parents (trio-based sequencing) was performed by the Beijing Genome Institute Europe using an Illumina HiSeq 4000 after enrichment for exons using the Agilent SureSelectXT Human All Exon 50 Mb kit (version 5). Read alignment (BWA), variant calling (GATK), variant annotation, and interpretation of variants were done by the Department of Genetics at the Radboud University Medical Center. Note that in F2:P1 a second variant was found in a noncoding region (intron) of *HAP1* (this variant is often found in WES, suggesting that it is a sequencing artifact).

Immunohistochemistry

To quantify the CSA of the slow-twitch and fast-twitch myofibers with conventional histochemical techniques, 10- μ m-thick cryostat sections were stained with nicotinamide adenine dinucleotide dehydrogenase (NADH) for F1:P1 and myofibrillar adenosine triphosphatase preincubated at pH 4.2 (mATPase 4.2) for control subjects and F2:P1. For NADH staining, the muscle sections were incubated with a 1:1 (v/v) mix of NADH solution (0.5 mg/mL NADH in 0.05 M Tris-HCl; pH 7.4) and nitrotetrazolium blue chloride (NBT) solution (2 mg/mL NBT in 0.05 M Tris-HCl; pH 7.4) for 1 hour at 37°C. The sections were then washed in increasing, followed by decreasing, acetone/H₂O solutions as follows: 30%, 60%, and 90%; followed by 90%, 60%, and 30%. The sections were then washed with dH₂O and coverslipped. For

mATPase 4.2, the muscle sections were thawed to room temperature for 1 hour and preincubated for 7 minutes at pH 4.2 in preincubation medium (acetate-barbiturate buffer solution, 0.1 M HCl, set to pH 4.2 with HCl). Next, the sections were incubated with incubation medium (0.5 M sodium barbital, 1.8 M CaCl₂, 5 μ M ATP, set to pH 9.4 with NaOH) at room temperature for 35 minutes and, after washing with CaCl₂, incubated with 0.5% ammonium sulfide for 1 minute. After counterstaining with phloxine and dehydration in xylene, the sections were coverslipped. To analyze the cross sections, open-source Fiji software was used to manually trace the circumference of the myofibers and calculate the Feret diameter (42).

Low-angle x-ray diffraction

Low-angle x-ray diffraction experiments were performed on the Biophysics Collaborative Access Team beamline 18ID at the Advanced Photon Source, Argonne National Laboratory (43). From F1:P1, 28 fibers were mounted and aligned in 1 plane between 2 halves of an EM grid and x-ray diffraction patterns were collected at a sarcomere length of 2.5 μ m, as described in the supplement material. The axial spacing of the Tn3 reflection at 12.7 nm and the sixth actin layer line at 5.9 nm was determined as described previously (44).

MD simulations

Human *TNNC2* with Ca²⁺ bound (holo) was modeled based on the *Oryctolagus cuniculus* holo (bound with 4 Ca²⁺ ions, 2 in each domain) TnC (*Tnc2*) x-ray crystal structure (PDB: 2TN4) (45). For modeling the human *TNNC2* Ca²⁺-free state (apo), we again used an *O. cuniculus* apo x-ray crystal structure (PDB: 1A2X) that was crystallized with a segment of C-terminal TnI (46). The CHARMM-GUI web server was used to build the solvated KCl-containing human *TNNC2* simulation systems (47). In total, 6 systems were built: 3 apo (Apo:WT, Apo:D34Y, and Apo:M79I) and 3 holo (Holo:WT, Holo:D34Y, and Holo:M79I). Each system was simulated via all-atom MD using the Amber 18 MD simulation engine and the input files for conducting MD simulations were generated using the CHARMM-GUI input generator (48, 49). The CHARMM36 all-atom additive force-field parameters were used to parameterize all components of the system (50). We collected approximately 18 μ s of simulation data using a 2-fs time step. Additional details, including those for MD simulations with the intact Tn complex (PDB: 1J1E), are in the supplemental material.

Myofiber contractility experiments

We adapted previously described methods to investigate the contractile properties of myofibers of patients (F1:P1, $n = 19$ fibers; F2:P1, $n = 22$ fibers) and healthy controls ($n = 6$, $n = 78$ fibers) (51–54). The protocol used in the current study is described in detail in the supplemental material. After completion of the protocol the myofibers were stored for analysis of myosin heavy chain isoform composition.

Protein expression and purification of fsTnC

Expression vectors encoding human WT and mutant (D34Y and M79I) TnC were transformed into *E. coli* to express the proteins. A detailed description of the protein expression and purification protocol can be found in the supplemental material.

Extraction and reconstitution of fsTnC in single permeabilized myofibers

Single myofibers were isolated and permeabilized as described above. We adapted previous methods (55) to reconstitute fsTnC in patient

and control myofibers. The protocol for the reconstitution and for the contractile measurements during the reconstitution experiments are described in detail in the supplemental material. After completion of the protocol the myofibers were stored for analysis of myosin heavy chain isoform composition.

Effect of tirasemtiv on myofiber contractility

We tested the ability of tirasemtiv, a fast skeletal muscle Tn activator, to augment the contractile force of patients' fast-twitch myofibers. Single myofibers were isolated and permeabilized as described above. The protocol was adapted from previous work (12). Details are in the supplemental material.

Myosin heavy chain isoform composition of permeabilized myofibers

Determination of the myosin heavy chain isoform composition of the single myofibers used in the contractility assays was performed as described previously (52, 56). Details are in the supplemental material.

Statistics

The quantified histology and myofiber contractility data were tested for significance by performing a mixed-model analysis with a random effect for biopsies and post hoc tests with Bonferroni's correction, after checking if the residues were normally distributed. The myofiber reconstitution and tirasemtiv data were tested for significance using a paired *t* test. Testing was performed using the software package SPSS Inc. (IBM). A *P* value of less than 0.05 was considered significant.

Study approval

Patient recruitment and sample collection. Written informed consents for study procedures and photographs were obtained from all human subjects by a qualified investigator (protocol 12-N-0095 approved by the IRB of the National Institute of Neurological Disorders and Stroke, NIH). Clinical exome sequencing by the Radboud University Medical Center was approved by the Medical Review Ethics Committee, Region Arnhem-Nijmegen, number 2011/188. The protocol for obtaining human biopsies from control subjects was approved by

the IRB at Amsterdam UMC (location VUmc) (number 2014/396) and written informed consent was obtained from the subjects.

Author contributions

MVDL, NV, CGB, and CACO conceived and designed the analyses, collected data, performed analyses, and wrote the manuscript. SD and TI collected data, performed analyses, and wrote the manuscript. JMDW and HG wrote the manuscript. SC, LB, and GS collected data. BK, PM, YH, LM, CQ, SAM, ARF, WM, EJK, KI, PHK, and JRP collected data and performed analyses. DTH and FIM provided compounds and wrote the manuscript.

Acknowledgments

We thank the families for participating in this study, and Christopher Mendoza and Gilberto ("Mike") Averion for their help in the clinic. We also thank the NIH Intramural Sequencing Center for performing the exome sequencing. The Ottenheijm laboratory is supported by a ZonMW-VICI grant (number 91819613), H2020-MSCA-RISE-2014 (64568 "Muscle Stress Relief"), and a Muscle Dystrophy UK grant (16NEM-PG36-0111). JRP is supported by the NHLBI/NIH award HL128683. HLG is supported by NIAMS/NIH R01AR053897. Work in the Bönnemann laboratory is supported by intramural funds from NINDS/NIH. Exome sequencing was funded through the Clinical Center Genomics Opportunity (CCGO), which is sponsored by the National Human Genome Research Institute (NHGRI), the NIH Deputy Director for Intramural Research, and the NIH Clinical Center. PKH was supported by the Maximizing Investigators' Research Award (MIRA) from NIGMS/NIH (R35GM124977) as well as supercomputer time from The Extreme Science and Engineering Discovery Environment (57). SAM is partially supported by the Iowa Wellstone Muscular Dystrophy Specialty Research Center (NINDS/NIH U54 NS053672).

Address correspondence to: Coen A.C. Ottenheijm, O2 Labgebouw, De Boelelaan 1108, 1081 HZ Amsterdam, The Netherlands. Phone: 31.0.20.4448123; Email: c.ottenheijm@amsterdamumc.nl.

- Gordon AM, et al. Regulation of contraction in striated muscle. *Physiol Rev.* 2000;80(2):853–924.
- Li A, et al. Skeletal MyBP-C isoforms tune the molecular contractility of divergent skeletal muscle systems. *Proc Natl Acad Sci USA.* 2019;116(43):21882–21892.
- Jungbluth H, et al. Congenital myopathies: disorders of excitation-contraction coupling and muscle contraction. *Nat Rev Neurol.* 2018;14(3):151–167.
- De Winter JM, et al. KBTBD13 is an actin-binding protein that modulates muscle kinetics. *J Clin Invest.* 2020;130(2):754–767.
- Solaro RJ. Troponin C – troponin I interactions and molecular signalling in cardiac myofilaments. *Adv Exp Med Biol.* 1995;382:109–115.
- Rarick HM, et al. The C terminus of cardiac troponin I is essential for full inhibitory activity and Ca²⁺ sensitivity of rat myofibrils. *J Biol Chem.* 1997;272(43):26887–26892.
- Chandra M, et al. The N-terminal region of troponin T is essential for the maximal activation of rat cardiac myofilaments. *J Mol Cell Cardiol.* 1999;31(4):867–880.
- Grabarek Z. Structural basis for diversity of the EF-hand calcium-binding proteins. *J Mol Biol.* 2006;359(3):509–525.
- Gifford JL, et al. Structures and metal-ion-binding properties of the Ca²⁺-binding helix-loop-helix EF-hand motifs. *Biochem J.* 2007;405(2):199–221.
- Oleszczuk M, et al. Solution structure of the regulatory domain of human cardiac troponin C in complex with the switch region of cardiac troponin I and W7: the basis of W7 as an inhibitor of cardiac muscle contraction. *J Mol Cell Cardiol.* 2010;48(5):925–933.
- Takeda S, et al. Structure of the core domain of human cardiac troponin in the Ca(2+)-saturated form. *Nature.* 2003;424(6944):35–41.
- de Winter JM, et al. Troponin activator augments muscle force in nemaline myopathy patients with nebulin mutations. *J Med Genet.* 2013;50(6):383–392.
- Richards S, et al. Standards and guidelines for the interpretation of sequence variants: a joint consensus recommendation of the American College of Medical Genetics and Genomics and the association for molecular pathology. *Genet Med.* 2015;17(5):405–424.
- Johnston JJ, et al. A novel nemaline myopathy in the Amish caused by a mutation in troponin T1. *Am J Hum Genet.* 2000;67(4):814–821.
- Sandaradura SA, et al. Nemaline myopathy and distal arthrogryposis associated with an autosomal recessive TNNT3 splice variant. *Hum Mutat.* 2018;39(3):383–388.
- Ilkovski B, et al. Nemaline myopathy caused by mutations in the muscle alpha-skeletal-actin gene. *Am J Hum Genet.* 2001;68(6):1333–1343.
- Laing NG, et al. A mutation in the alpha tropomyosin gene TPM3 associated with autosomal dominant nemaline myopathy. *Nat Genet.* 1995;9(1):75–79.
- Donner K, et al. Mutations in the beta-tropomyosin (TPM2) gene—a rare cause of nemaline myopathy. *Neuromuscul Disord.* 2002;12(2):151–158.
- Pelin K, et al. Mutations in the nebulin gene associ-

- ated with autosomal recessive nemaline myopathy. *Proc Natl Acad Sci USA.* 1999;96(5):2305–2310.
20. Yuen M, et al. Leiomodin-3 dysfunction results in thin filament disorganization and nemaline myopathy. *J Clin Invest.* 2015;125(1):456–457.
 21. Agrawal PB, et al. Nemaline myopathy with minicores caused by mutation of the CFL2 gene encoding the skeletal muscle actin-binding protein, cofilin-2. *Am J Hum Genet.* 2007;80(1):162–167.
 22. Malfatti E, et al. A premature stop codon in MYO18B is associated with severe nemaline myopathy with cardiomyopathy. *J Neuromuscul Dis.* 2015;2(3):219–227.
 23. Miyatake S, et al. Biallelic mutations in MYPN, encoding myopalladin, are associated with childhood-onset, slowly progressive nemaline myopathy. *Am J Hum Genet.* 2017;100(1):169–178.
 24. Ravenscroft G, et al. Mutations in KLHL40 are a frequent cause of severe autosomal-recessive nemaline myopathy. *Am J Hum Genet.* 2013;93(1):6–18.
 25. Gupta VA, et al. Identification of KLHL41 mutations implicates BTB-Kelch-mediated ubiquitination as an alternate pathway to myofibrillar disruption in nemaline myopathy. *Am J Hum Genet.* 2013;93(6):1108–1117.
 26. Sambuughin N, et al. Dominant mutations in KBTBD13, a member of the BTB/Kelch family, cause nemaline myopathy with cores. *Am J Hum Genet.* 2010;87(6):842–848.
 27. Schiaffino S, Reggiani C. Fiber types in mammalian skeletal muscles. *Physiol Rev.* 2011;91(4):1447–1531.
 28. Hoh JFY. Laryngeal muscle fibre types. *Acta Physiol Scand.* 2005;183(2):133–149.
 29. Sung SS, et al. Mutations in genes encoding fast-twitch contractile proteins cause distal arthrogryposis syndromes. *Am J Hum Genet.* 2003;72(3):681–690.
 30. Li C, Samulski RJ. Engineering adeno-associated virus vectors for gene therapy. *Nat Rev Genet.* 2020;21(4):255–272.
 31. Salabarria SM, et al. Advancements in AAV-mediated gene therapy for pompe disease. *J Neuromuscul Dis.* 2020;7(1):15–31.
 32. Kimura T, et al. Production of adeno-associated virus vectors for in vitro and in vivo applications. *Sci Rep.* 2019;9(1):13601.
 33. Russell AJ, et al. Activation of fast skeletal muscle troponin as a potential therapeutic approach for treating neuromuscular diseases. *Nat Med.* 2012;18(3):452–455.
 34. Haus JM, et al. Contractile and connective tissue protein content of human skeletal muscle: effects of 35 and 90 days of simulated microgravity and exercise countermeasures. *Am J Physiol Regul Integr Comp Physiol.* 2007;293(4):R1722–R1727.
 35. Hwee DT, et al. Fast skeletal muscle troponin activator tirasemtiv increases muscle function and performance in the B6SJL-SOD1G93A ALS mouse model. *PLoS One.* 2014;9(5):e96921.
 36. Lee EJ, et al. Functional characterization of the intact diaphragm in a nebulin-based nemaline myopathy (NM) model—effects of the fast skeletal muscle troponin activator tirasemtiv. *Int J Mol Sci.* 2019;20(20):5008.
 37. Shefner JM, et al. A phase III trial of tirasemtiv as a potential treatment for amyotrophic lateral sclerosis. *Amyotroph Lateral Scler Front Degener.* 2019;20(7–8):584–594.
 38. Andrews JA, et al. CK-2127107 amplifies skeletal muscle response to nerve activation in humans. *Muscle Nerve.* 2018;57(5):729–734.
 39. Shefner JM, et al. A phase 2, double-blind, randomized, dose-ranging trial of reldesemtiv in patients with ALS [published online September 24, 2020]. *Amyotroph Lateral Scler Front Degener.* <https://doi.org/10.1080/21678421.2020.1822410>.
 40. Teer JK, et al. VarSifter: visualizing and analyzing exome-scale sequence variation data on a desktop computer. *Bioinformatics.* 2012;28(4):599–600.
 41. Karczewski KJ, et al. The mutational constraint spectrum quantified from variation in 141,456 humans. *Nature.* 2020;581(7809):434–443.
 42. Schindelin J, et al. Fiji: an open-source platform for biological-image analysis. *Nat Methods.* 2012;9(7):676–682.
 43. Fischetti R, et al. The BioCAT undulator beamline 18ID: a facility for biological non-crystalline diffraction and x-ray absorption spectroscopy at the Advanced Photon Source. *J Synchrotron Radiat.* 2004;11(pt 5):399–405.
 44. Wakabayashi K, et al. X-ray diffraction evidence for the extensibility of actin and myosin filaments during muscle contraction. *Biophys J.* 1994;67(6):2422–2435.
 45. Houdusse A, et al. Structures of four Ca^{2+} -bound troponin C at 2.0 Å resolution: further insights into the Ca^{2+} -switch in the calmodulin superfamily. *Structure.* 1997;5(12):1695–1711.
 46. Vassilyev DG, et al. Crystal structure of troponin C in complex with troponin I fragment at 2.3-A resolution. *Proc Natl Acad Sci U.S.A.* 1998;95(9):4847–4852.
 47. Jo S, et al. CHARMM-GUI: a web-based graphical user interface for CHARMM. *J Comput Chem.* 2008;29(11):1859–1865.
 48. Case DA, et al. AMBER 2020, University of California, San Francisco. <https://ambermd.org/CiteAmber.php>.
 49. Lee J, et al. CHARMM-GUI input generator for NAMD, GROMACS, AMBER, OpenMM, and CHARMM/OpenMM simulations using the CHARMM36 additive force field. *J Chem Theory Comput.* 2016;12(1):405–413.
 50. Huang J, et al. CHARMM36m: an improved force field for folded and intrinsically disordered proteins. *Nat Methods.* 2016;14(1):71–73.
 51. van de Locht M, et al. Recessive MYH7-related myopathy in two families. *Neuromuscul Disord.* 2019;29(6):456–467.
 52. Joureau B, et al. Dysfunctional sarcomere contractility contributes to muscle weakness in ACTA1-related nemaline myopathy (NEM3). *Ann Neurol.* 2018;83(2):269–282.
 53. Winter JM de, et al. Mutation-specific effects on thin filament length in thin filament myopathy. *Ann Neurol.* 2016;79(6):959–969.
 54. Ottenheijm CAC, et al. Deleting exon 55 from the nebulin gene induces severe muscle weakness in a mouse model for nemaline myopathy. *Brain.* 2013;136(pt 6):1718–1731.
 55. Veltri T, et al. Amide hydrogens reveal a temperature-dependent structural transition that enhances site-II Ca^{2+} -binding affinity in a C-domain mutant of cardiac troponin C. *Sci Rep.* 2017;7(1):691.
 56. Ottenheijm CA, et al. Thin filament length dysregulation contributes to muscle weakness in nemaline myopathy patients with nebulin deficiency. *Hum Mol Genet.* 2009;18(13):2359–2369.
 57. Towns J, et al. XSEDE: accelerating scientific discovery. *Comput Sci Eng.* 2014;16(5):62–74.
 58. Servier. SMART — Servier Medical ART. <https://smart.servier.com/>. Accessed March 22, 2021.
 59. Wittenbach JD, et al. MuscleViz: free open-source software for muscle weakness visualization. *J Neuromuscul Dis.* 2019;6(2):263–266.